

Stardust Interstellar Preliminary Examination VII: Synchrotron X-ray fluorescence analysis of six Stardust interstellar candidates measured with the Advanced Photon Source 2-ID-D microprobe

George J. FLYNN^{1*}, Steven R. SUTTON^{2,3}, Barry LAI², Sue WIRICK³, Carlton ALLEN⁴, David ANDERSON⁵, Asna ANSARI⁶, Saša BAJT⁷, Ron K. BASTIEN⁴, Nabil BASSIM⁸, Hans A. BECHTEL⁹, Janet BORG¹⁰, Frank E. BRENKER¹¹, John BRIDGES¹², Donald E. BROWNLEE¹³, Mark BURCHELL¹⁴, Manfred BURGHAMMER¹⁵, Anna L. BUTTERWORTH⁵, Hitesh CHANGELA¹⁶, Peter CLOETENS¹⁵, Andrew M. DAVIS¹⁷, Ryan DOLL¹⁸, Christine FLOSS¹⁸, David FRANK⁴, Zack GAINSFORTH⁵, Eberhard GRÜN¹⁹, Philipp R. HECK⁶, Jon K. HILLIER²⁰, Peter HOPPE²¹, Bruce HUDSON²², Joachim HUTH²¹, Brit HVIDE⁶, Anton KEARSLEY²³, Ashley J. KING²⁴, Jan LEITNER²¹, Laurence LEMELLE²⁵, Hugues LEROUX²⁶, Ariel LEONARD¹⁸, Robert LETTIERI⁵, William MARCHANT⁵, Larry R. NITTLER²⁷, Ryan OGLIORE²⁸, Wei Ja ONG¹⁸, Frank POSTBERG²⁰, Mark C. PRICE¹⁴, Scott A. SANDFORD²⁹, Juan-Angel Sans TRESSERAS¹⁵, Sylvia SCHMITZ¹¹, Tom SCHOONJANS³⁰, Geert SILVERSMIT³⁰, Alexandre SIMONOVICI³¹, Vicente A. SOLÉ¹⁵, Ralf SRAMA³², Frank J. STADERMANN¹⁸, Thomas STEPHAN¹⁷, Veerle STERKEN^{33,34,35}, Julien STODOLNA⁵, Rhonda M. STROUD³⁶, Mario TRIELOFF²⁰, Peter TSOU³⁷, Akira TSUCHIYAMA³⁸, Tolek TYLISZCZAK⁹, Bart VEKEMANS³⁰, Laszlo VINCZE³⁰, Joshua VON KORFF⁵, Andrew J. WESTPHAL⁵, Naomi WORDSWORTH³⁹, Daniel ZEVIN⁵, Michael E. ZOLENSKY⁴, and >30,000 Stardust@home dusters⁴⁰

¹SUNY Plattsburgh, Plattsburgh, New York, USA

²Advanced Photon Source, Argonne National Laboratory, Chicago, Illinois, USA

³CARS, University of Chicago, Chicago, Illinois, USA

⁴ARES, NASA JSC, Houston, Texas, USA

⁵Space Sciences Laboratory, U.C. Berkeley, Berkeley, California, USA

⁶Robert A. Pritzker Center for Meteoritics and Polar Studies, The Field Museum of Natural History, Chicago, Illinois, USA

⁷DESY, Hamburg, Germany

⁸Naval Research Laboratory, Washington, District of Columbia, USA

⁹Advanced Light Source, Lawrence Berkeley Laboratory, Berkeley, California, USA

¹⁰IAS Orsay, Orsay, France

¹¹Geoscience Institute, Goethe University Frankfurt, Frankfurt, Germany

¹²Space Research Centre, University of Leicester, Leicester, UK

¹³Department of Astronomy, University of Washington, Seattle, Washington, USA

¹⁴University of Kent, Kent, UK

¹⁵European Synchrotron Radiation Facility, Grenoble, France

¹⁶George Washington University, Washington, District of Columbia, USA

¹⁷The University of Chicago, Chicago, Illinois, USA

¹⁸Washington University, St. Louis, Missouri, USA

¹⁹Max-Planck-Institut für Kernphysik, Heidelberg, Germany

²⁰Institut für Geowissenschaften, Universität Heidelberg, Heidelberg, Germany

²¹Max-Planck-Institut für Chemie, Mainz, Germany

²²ISPE Duster, Ontario, Canada

²³Natural History Museum, London, UK

²⁴The University of Chicago and Robert A. Pritzker Center for Meteoritics and Polar Studies, The Field Museum of Natural History, Chicago, Illinois, USA

²⁵Ecole Normale Supérieure de Lyon, Lyon, France

²⁶Laboratoire de Structure et Propriétés de l'Etat Solide, UMR CNRS 8008, Université des Sciences et Technologies de Lille, F-59655 Villeneuve d'Ascq-Cedex, France

²⁷Carnegie Institution of Washington, Washington, District of Columbia, USA

²⁸University of Hawai'i at Manoa, Honolulu, Hawaii, USA

²⁹NASA Ames Research Center, Moffett Field, California, USA

³⁰University of Ghent, Ghent, Belgium

³¹Institut des Sciences de la Terre, Observatoire des Sciences de l'Univers de Grenoble, Grenoble, France

³²Institut für Raumfahrtssysteme, Universität Stuttgart, Stuttgart, Germany

³³Universität Stuttgart, Stuttgart, Germany

³⁴Institute for Geophysics and Extraterrestrial Physics, TU Braunschweig, Braunschweig, Germany

³⁵Max-Planck-Institut für Kernphysik, Heidelberg, Germany

³⁶Materials Science and Technology Division, Naval Research Laboratory, Washington, District of Columbia, USA

³⁷Jet Propulsion Laboratory, Pasadena, California, USA

³⁸Osaka University, Osaka, Japan

³⁹South Buckinghamshire, UK

⁴⁰Worldwide

*Corresponding author. E-mail: flynnngi@plattsburgh.edu

(Received 11 December 2012; revision accepted 15 May 2013)

Abstract—The NASA Stardust spacecraft exposed an aerogel collector to the interstellar dust passing through the solar system. We performed X-ray fluorescence element mapping and abundance measurements, for elements $19 \leq Z \leq 30$, on six “interstellar candidates,” potential interstellar impacts identified by Stardust@Home and extracted for analyses in picokeystones. One, I1044,3,33, showed no element hot-spots within the designated search area. However, we identified a nearby surface feature, consistent with the impact of a weak, high-speed particle having an approximately chondritic (CI) element abundance pattern, except for factor-of-ten enrichments in K and Zn and an S depletion. This hot-spot, containing approximately 10 fg of Fe, corresponds to an approximately 350 nm chondritic particle, small enough to be missed by Stardust@Home, indicating that other techniques may be necessary to identify all interstellar candidates. Only one interstellar candidate, I1004,1,2, showed a track. The terminal particle has large enrichments in S, Ti, Cr, Mn, Ni, Cu, and Zn relative to Fe-normalized CI values. It has high Al/Fe, but does not match the Ni/Fe range measured for samples of Al-deck material from the Stardust sample return capsule, which was within the field-of-view of the interstellar collector. A third interstellar candidate, I1075,1,25, showed an Al-rich surface feature that has a composition generally consistent with the Al-deck material, suggesting that it is a secondary particle. The other three interstellar candidates, I1001,1,16, I1001,2,17, and I1044,2,32, showed no impact features or tracks, but allowed assessment of submicron contamination in this aerogel, including Fe hot-spots having CI-like Ni/Fe ratios, complicating the search for CI-like interstellar/interplanetary dust.

INTRODUCTION

Stardust, the fourth NASA Discovery mission, collected and delivered to Earth dust particles from comet 81P/Wild 2 (Brownlee et al. 2006). As a second mission objective, the Stardust spacecraft collected contemporary interstellar grains passing through the solar system. The Stardust Interstellar Dust Collector (SIDC), approximately 1039 cm² of aerogel cells similar to those employed for the collection of the comet Wild 2 dust, was exposed to the interstellar dust stream for 195 days while the spacecraft was flying approximately opposite the direction of the Sun's motion through the local interstellar medium (ISM), thus minimizing the capture speed for the interstellar dust (Westphal et al. 2014b).

Astronomical observations provide constraints on the size, the elemental composition, and the mineralogy of interstellar dust particles. Depletions of refractory elements in the interstellar gas indicate that Si, Mg, Mn, Cr, Fe, and Ni are major elements in the condensed dust phase (Savage and Sembach 1996). However, these same observations indicate that some of the moderately volatile elements (e.g., S) remain mostly in the gas phase (Savage and Sembach 1996). Thus, on average, interstellar dust is likely to consist of the major rock-forming elements in ratios similar to those in CI meteorites, but it should be depleted in some moderately volatile elements (e.g., S).

As many solids exhibit bending, wagging, or stretching modes in the infrared region of the spectrum, infrared spectroscopy has been used to constrain the

mineralogy of the interstellar dust. Infrared measurements show that interstellar dust has a strong, broad emission feature near 10 μm , consistent with amorphous silicate, and several weaker features near 3.4 μm , consistent with aliphatic C-H₂ and C-H₃ stretching absorptions (Whittet et al. 1997). As crystalline silicates have sharp features near 10 μm , Kemper et al. (2004) placed an upper limit on the crystalline to amorphous silicate ratio in interstellar grains of approximately 0.2%. However, these elemental and mineralogical observations relate to the bulk properties of the interstellar dust, so none of these observations constrain the properties of any individual interstellar dust particle.

Ancient interstellar dust that was trapped in meteorites and interplanetary dust particles exhibits a wide range of elemental compositions and mineralogies, including amorphous and crystalline silicates (Messenger et al. 2005), SiC, graphite, silicon nitride, corundum, spinel, and hibonite (Clayton and Nittler 2004). However, these grains were identified because they preserve unusual isotopic compositions representative of their specific formation environments. They may not be representative of the majority of interstellar grains, which are likely to have been processed in the ISM, undergoing destruction and recondensation (Jones et al. 1996; Zhukovska et al. 2008). These processes can mix material from different sources, minimizing or eliminating the distinct isotopic signatures of their individual sources. However, estimates of the O isotopic composition of the local ISM (Wilson 1999) are distinct from the solar system value, so interstellar grains that recondensed in the local ISM likely record that distinct O isotopic signature.

Measurements by dust detectors on the Ulysses and Galileo spacecraft indicate that the diameter of the dust particles entering the inner solar system from the local ISM is peaked near 0.5 μm (Krüger et al. 2007). So, any interstellar grains collected by Stardust would be much smaller, less than 1/1000th the mass, than the smallest Wild 2 grains analyzed by X-ray fluorescence (XRF) during the Wild 2 preliminary examination (Flynn et al. 2006), making their identification and characterization significantly more challenging.

As planetary differentiation segregated much of the Earth's Ni into the core, the Ni/Fe ratio can frequently be used to distinguish unprocessed extraterrestrial material, such as primitive CI meteorites with Ni/Fe approximately 1/18, from terrestrial surface material, which has a much lower average Ni/Fe. Fe, a major element in the condensed phase (dust) in the ISM, and Ni are both easily detected and quantified using X-ray microprobes (XRMs), so Fe-mapping may be an efficient way to search for the most common interstellar

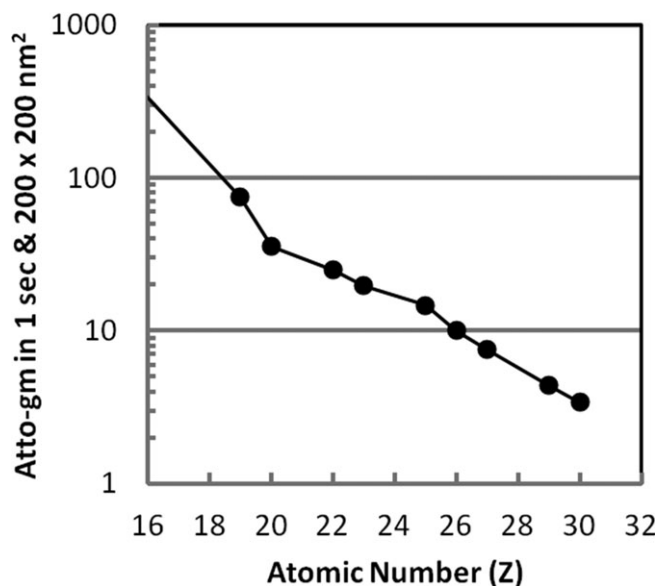


Fig. 1. Detection limits, in attograms, of the 2-ID-D X-ray microprobe for 1 s data acquisition time with a 200 nm focused beam spot.

or interplanetary dust particles captured in the SIDC, and the Ni/Fe ratio might provide a way to distinguish extraterrestrial material from terrestrial dust.

We report here measurements of heavy element abundances in six interstellar dust candidate features from the SIDC made with an XRM beamline, 2-ID-D, at the Advanced Photon Source (APS) at Argonne National Laboratory. This facility-managed beamline is devoted to high-resolution (submicrometer) X-ray imaging studies. The X-ray source is the 3.3 cm period Undulator A, which covers the energy range from 4 to 13 keV in the first harmonic with high X-ray brilliance. Zone plate optics (chromatic) are used to focus the X-ray beam from a Kohzu Si(111) monochromator to a spot size of approximately 250 nm (full-width half-maximum) with a flux of approximately 4×10^9 photons s^{-1} at 10 keV. To produce element maps, the sample is raster scanned through the X-ray beam and XRF spectra are acquired at each pixel in the scan. As the X-ray beam passes through the entire thickness of the samples employed in this study, this technique cannot distinguish between contamination on the surfaces of the aerogel picrokeystones and particles in the interior of the aerogel.

The XRF detector is a Vortex silicon drift diode (energy-dispersive) operated in a helium-purged sample environment, used to enhance sensitivity for light elements. Detection limits vary from element to element. The detection limits for a 1-second count time on an individual pixel for elements from atomic number $Z = 19$ (K) to $Z = 30$ (Zn) are shown in Fig. 1. A general description of the instrument and the determination of

the element detection limits are given, for a very similar instrument on beamline 2-ID-E of the APS, in Twining et al. (2003). However, the aerogel itself contains detectable levels of Si, S, Cl, Ti, Mn, Fe, Ni, Cu, and Zn, which vary from spot to spot, thus raising our detection limits for these elements in captured material.

SAMPLES AND MEASUREMENTS

The space-exposed surface of each Stardust interstellar aerogel cell was optically scanned at the NASA Johnson Space Center (JSC) Curatorial Facility, and potential interstellar impact features visible on the space-exposed surface of aerogel cells in the SIDC were identified by participants in the Stardust@Home project (<http://stardustathome.ssl.berkeley.edu>), described in Westphal et al. (2014a). The number of interstellar candidate features identified by the Stardust@Home project is significantly greater than the number of interstellar grain impacts expected based the Galileo and Ulysses measurements and on modeling of the interstellar flux (Westphal et al. 2014b). This excess largely results from the collection of secondary particles produced by impacts of interplanetary or interstellar dust on the Stardust solar panels or parts of the Stardust sample return capsule, both of which were within the field of view of the SIDC, the direct capture of interplanetary dust particles, or the misidentification of features produced during preparation of the aerogel. A major objective of the Stardust Interstellar Preliminary Examination (ISPE) was to perform nondestructive characterization of the interstellar candidates in order to identify secondary particles, based on the elemental compositions of spacecraft hardware within the field of view of the collector, and to compare the compositions of features not identified as spacecraft secondary particles with the known or expected properties of interstellar dust. As destructive analyses, such as isotopic measurements, were not permitted during the ISPE, it is anticipated that particles not compellingly identified as spacecraft secondary material will be made available through the NASA JSC Curatorial Facility for more comprehensive characterization by other techniques.

Aerogel picokeystones (Fig. 2) containing these interstellar candidate features were extracted from the aerogel cells by the NASA JSC Curatorial Facility in picokeystones, wedge-shaped volumes of aerogel machined from the aerogel cell using glass needles controlled by automatic micromanipulators (Frank et al. 2013). Each picokeystone was sandwiched between two silicon nitride windows, protecting the sample from damage, loss, or contamination, and permitting all of the synchrotron-based analytical techniques performed during the ISPE (Frank et al. 2013).

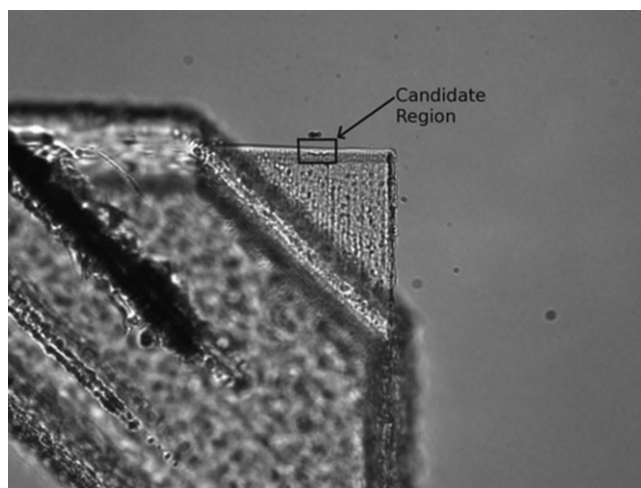


Fig. 2. Aerogel interstellar picokeystone I1044,2,32,0,0 after extraction from the Stardust interstellar collector. The image is 1170 μm wide.

We were allocated six interstellar candidate picokeystones (I1004,1,2; I1001,1,16; I1001,2,17; I1044,2,32; I1044,3,33; and I1075,1,25), and we were provided with optical microscope side-view images annotated with the interstellar “candidate region” (Fig. 2), where the Stardust@Home project identified a possible particle track from examination of the top-view optical images. We performed XRF element mapping and element abundance analysis on each of the six samples at beam line 2-ID-D at the APS.

We first mapped the entire candidate region and some surrounding area at low spatial resolution, with step sizes as large as 1 μm , taking advantage of the wings of the X-ray distribution around the approximately 250 nm x-ray beam hot-spot to fluoresce major elements in captured particles over the full 1 μm pixel (Fig. 3). Once element hot-spots were identified, higher resolution XRF images, in steps as small as 100 nm, were collected.

For each picokeystone, we collected a data set consisting of a full, 2048-channel XRF spectrum at each pixel in the mapped area. Element maps were obtained by defining an energy range corresponding to the position of the K-line fluorescence of each element of interest and plotting the XRF signal intensity at each pixel in the map. Each element map was scaled so the brightest pixel in the image corresponded to the maximum counts for that element.

Several regions of interest (ROI) were defined on each high-resolution map to include: (1) each object of interest and (2) an area of background pixels as far from the object of interest as possible (Fig. 3). Integrated XRF spectra were obtained for each ROI by summation of the full XRF spectra in each of the included pixels. The concentration of each element in an

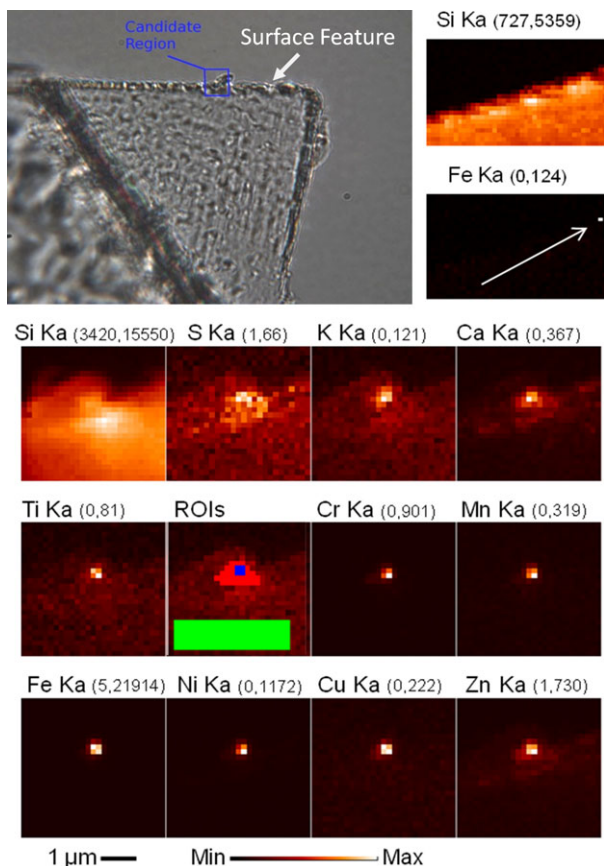


Fig. 3. Top: Visible light image (420 μm width) of interstellar candidate I1044,3,33. Right: Coarse elemental maps (100 μm width) for Si and Fe centered on the candidate region. Only a Fe hot-spot (arrow) not associated with the candidate object was observed. Bottom: X-ray fluorescence element maps of the Fe hot-spot area showing a single hot-spot for most of the elements analyzed. Values in parentheses are the minimum and maximum counts used in applying the color scale bar. The “ROIs” image shows the locations of the three integration regions, entire particle (red + blue), restricted particle (blue), and background (green).

ROI was obtained by peak fitting and conversion into $\mu\text{g cm}^{-2}$ using measurements on the NIST SRM 1832 and 1833 thin film standards.

To reach the detector, the fluorescence X-rays passed through one of the silicon nitride windows protecting the delicate picokeystones from contamination and damage. Each window was either 50 nm or 70 nm thick. The data reduction procedures corrected for the absorption of fluorescence X-rays by this window, assuming Si_3N_4 with a density of 3.44 g cm^{-3} and a 100 nm thickness at a take-off angle of 15° , the tilt of the sample relative to the incident X-ray beam in the Sector 2-ID-D XRM. The maximum window absorption correction was 15% for sulfur. No attempt was made to make self-absorption corrections for the aerogel picokeystones, which will only

significantly affect elements having a lower Z than Ca, because the depth distribution of the elements within the picokeystone is not known. However, by overestimating the thickness of the silicon nitride windows, we correct for the absorption of approximately $5 \mu\text{m}$ of overlying aerogel having a density of 26 mg cm^{-3} .

As the Stardust aerogel cells contain significant contamination (Flynn et al. 2006) for many elements, background quantification and subtraction are required. Two different approaches for background subtraction were used: (1) Pixel normalization where the integrated XRF spectrum for the background ROI was scaled to the same number of pixels as that of the object ROI, followed by spectral subtraction, fitting of the net spectrum, and conversion into $\mu\text{g cm}^{-2}$; (2) Si K-alpha normalization where the XRF spectrum of the background ROI was scaled to match that of the object ROI in the Si K-alpha region of the spectrum, followed by spectral subtraction, fitting of the net spectrum, and conversion into $\mu\text{g cm}^{-2}$. The former approach assumes that the aerogel contamination contribution is the same at each pixel, an approach that does not take into account contributions from compressed or melted aerogel, both of which were identified associated with the comet particles captured by Stardust (Brownlee et al. 2006). The latter approach assumes all the silicon in the object area derives from aerogel, whether compressed or not, which should overestimate the contamination provided it is uniform throughout the aerogel. The contribution to the measured Si K fluorescence intensity from Si atoms in the silicon nitride window was small compared with that from Si atoms in the aerogel picokeystone (approximately 10 versus $300 \mu\text{g cm}^{-2}$).

Element/Fe ratios were then calculated for each object of interest. These ratios were compared with those for the CI chondrite meteorites (Lodders 2003).

RESULTS

Here, we describe the six individual picokeystones that we analyzed at the APS, including their XRF maps and spectra and the derived element abundance patterns. Only one of these six picokeystones, I1004,1,2, showed a track with a terminal particle in the side-view optical image provided by the JSC Curatorial Facility. As a major objective of the ISPE is to identify secondary fragments, where appropriate, we compare the compositions of the objects of interest with the two largest spacecraft components within the field of view of the interstellar collector: the solar panels, which can be identified by detectable Ce and Zn; and the aluminum deck of the Stardust sample return capsule, which was sampled and analyzed by XRF.

I1044,3,33

The visible light image of I1044,3,33 showed no obvious track or terminal particle in the side-view optical image taken at the JSC Curatorial Facility after picokeystone extraction (Fig. 3). Based on the position from which the picokeystone was extracted, the JSC Curatorial Facility identified a “candidate region” for our XRM search. Low-resolution XRF element mapping of a 100 μm strip along the space-exposed edge of the picokeystone showed no element hot-spots within the “candidate region” (Fig. 3), located about 70 μm from the tip of the picokeystone. However, we did identify an Fe concentration in a spot along the space-exposed edge of the picokeystone, well outside of the interstellar candidate region. This hot-spot is located about 30 μm from the tip of the picokeystone (Fig. 3).

High-resolution element mapping, with a step size of 150 nm and a dwell time of 1 s per pixel, of this feature identified a single hot-spot for most of the elements analyzed (Fig. 3). There are four high count pixels, encompassing a 300 nm diameter hot-spot, and a surrounding halo about 1 μm across. Integrated spectra were obtained separately for this full 1 μm region and the smaller core area. The aerogel background spectrum, shown in green in Fig. 4, demonstrates that the aerogel itself contains detectable amounts of Si, S, Cl, Ca, Ti, Mn, Fe, Ni, Cu, and Zn. However, the XRF spectra of the core and the halo of this feature are both quite distinct from the spectrum of the background area (Fig. 4), with large excesses of S, Ca, Cr, Mn, Fe, Ni, Cu, and Zn in the core and the halo areas compared with the spectrum of the background area scaled to the same number of pixels as the core area, demonstrating that we have good sensitivity for these elements with a 1 s per pixel dwell time. The element abundance patterns of the core and the entire approximately 1 μm area are quite similar to each other, and each shows a nearly flat (CI-like) pattern, with the exception of elevated K and Zn (each about a factor of 10 higher than CI) and a large depletion in S. The nearly flat, CI-like, pattern for most elements is consistent with the observed mean composition of interplanetary dust particles, and the expected mean composition of interstellar dust. Elevated K and Zn (Sutton and Flynn 1988) have been reported in some interplanetary dust particles, resulting from the presence of rare, Zn- or K-rich minerals. Similar effects might also occur in rare interstellar grains, although on average the ISM is depleted in moderately volatile elements (Savage and Sembach 1996). This elemental composition fails to resolve the origin of this particle.

Because the solar panels and the aluminum deck of the sample return capsule are within the field of view

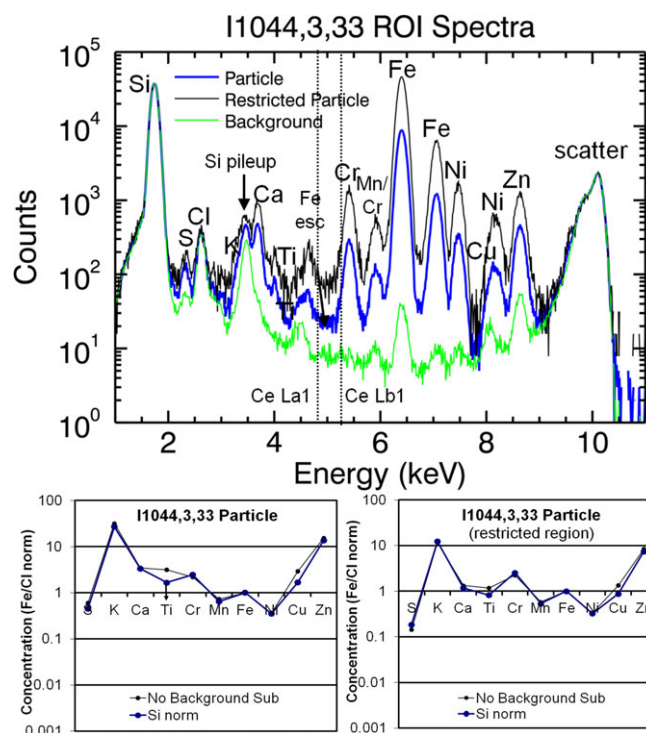


Fig. 4. X-ray fluorescence spectra of the whole hot-spot (“particle,” blue), the core of the Fe hot-spot (“restricted particle,” black), and the background region (green). Cerium was not detected as evidenced by the lack of peaks at the major Ce L fluorescence energies (vertical dashed lines). The CI- and Fe-normalized element abundance patterns for both regions are shown below the spectra. Downward arrows indicate detection limits for elements that were not detected. The counts in the restricted particle and background spectra were scaled to the same number of pixels as the particle spectrum.

of the SIDC, we examined the XRF spectra for the Ce L-lines, which should be easily detectable, and for Al. The spectra show no detectable Ce, which would appear at the positions of the dashed vertical lines in Fig. 4, ruling out the solar panels as a source of this material, and no detectable Al, suggesting that the aluminum deck is not the source of this material.

Summing over the four highest intensity pixels in the Fe map, a square region approximately 300 nm on a side, gives a total Fe mass of 10 fg. A sphere of chondritic composition (18.5% Fe) with this Fe mass would be about 350 nm in diameter, consistent with the observed interstellar dust size distribution. The feature is not at the end of a track, but could result from the high-speed impact of a porous particle.

There is no obvious directionality in the element distributions observed in the X-ray images (Fig. 3) because the feature is only approximately 2×2 pixels in size. However, subsequent higher resolution images

made using a scanning transmission X-ray microscope (STXM) at the Advanced Photon Source revealed a morphology consistent with the impact of a high-speed projectile, and suggested a possible impact direction (Butterworth et al. 2014). Based on the orientation of the picokeystone in the aerogel cell, this impact direction is not consistent with either a “midnight” or a “6 o’clock” impact, the two most likely orientations for an interstellar impact (Sterken et al. 2014; Westphal et al. 2014b). While not completely ruling out an interstellar origin, this orientation suggests that if the feature in I1044,3,33 is an impact, then it probably results from the impact of an interplanetary dust particle.

Although the optical scanning employed in the Stardust@Home project has successfully identified several potential interstellar impacts (Westphal et al. 2014a), this possible impact feature was not identified by the Stardust@Home optical scanning. The feature is located approximately 40 μm from the area identified as the candidate region (Fig. 3). The failure to detect this surface feature by the Stardust@Home project may result from the small size of the possible impactor. Postberg et al. (2014) showed that analog shots of particles $<0.4 \mu\text{m}$ in diameter with capture speeds below 6 km s^{-1} have low detection efficiency by optical microscopy.

Our observation, combined with the results of Postberg et al. (2014), suggest that a parallel effort to identify very small impact features in the SIDC by an alternative technique is desirable. One possibility to detect these small features is to employ Fe-mapping (Flynn et al. 2009). An $0.3\text{--}0.5 \mu\text{m}$ diameter interstellar or interplanetary particle with a CI-like Fe content would easily be detectable by Fe mapping using an XRM with a relatively large beam spot, e.g., approximately $3\text{--}10 \mu\text{m}$ in diameter. The particle can then be located in three dimensions using a simplified computed microtomography technique, raster-scanning an aerogel block at three different rotation angles, and recording the positions of Fe hot-spots. If there are only a few Fe hot-spots in the aerogel block, the locations of these hot-spots can be determined by triangulation (Flynn et al. 2009).

I1001,1,16

The visible light image of I1001,1,16 shows a feature, possibly a “crater” resulting from a high-velocity impact, as well as a fracture in the aerogel (Fig. 5). As with I1044,3,33, this interstellar candidate is a surface feature with no obvious track. An XRF map showed that the surface feature consists of a $4 \times 10 \mu\text{m}$ Si-rich region containing three much smaller element hot-spots, two containing a significant amount of Fe

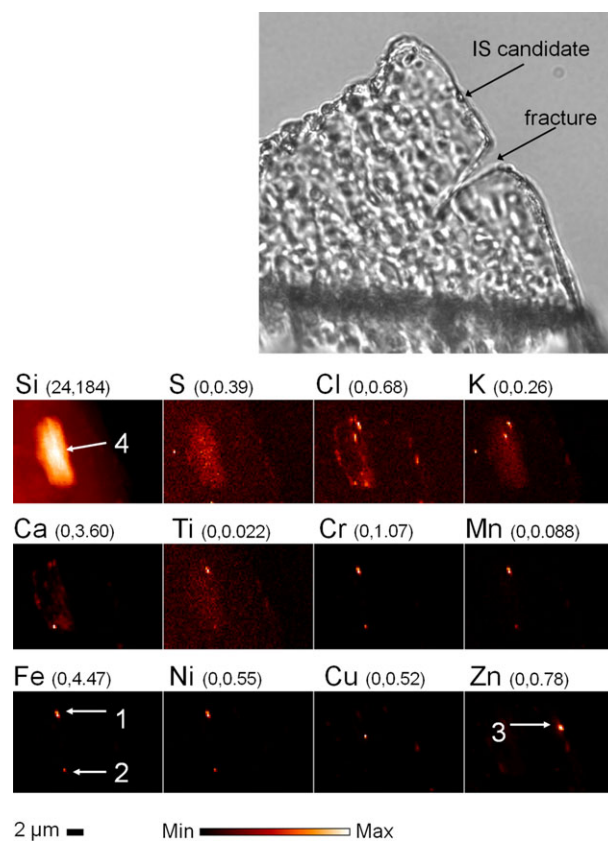


Fig. 5. Right: Visible light image (600 μm width) of interstellar candidate I1001,1,16, showing a large crack as well as the interstellar candidate feature (from Stardust Interstellar Preliminary Examination wiki). Bottom: X-ray fluorescence element maps of interstellar candidate I1001,1,16 showing a surface feature that consists of a $4 \times 10 \mu\text{m}$ Si-rich region containing three small element hot-spots, two rich in Fe and the third rich in Zn. Values in parentheses are the minimum and maximum $\mu\text{g cm}^{-2}$ used in applying the color scale bar.

and the third containing Zn (Fig. 5). The three element hot-spots as well as the entire Si-rich region were selected for higher resolution data collection.

The two Fe hot-spots, Objects 1 and 2, have similar element abundance patterns (Fig. 6), with the Mn/Fe and Ni/Fe ratios plotting near CI, but showing large enrichments over CI in all the other elements measured except for S, Ti, and, in the case of Object 1, Ca. The Zn hot-spot, Object 3, despite its very low Fe content, shows the same flat pattern of Mn/Fe and Ni/Fe, but large enrichments in all other detected elements. The large Si-rich area was integrated over about half its volume not including the two Fe hot-spots. Its pattern is similar to that of the Zn hot-spot. The Si-normalized element abundance pattern is distinctly different from the aerogel contamination pattern, suggesting that the Si-rich region is not simply compressed aerogel. As Object 1 is simply embedded in a high-density Si region,

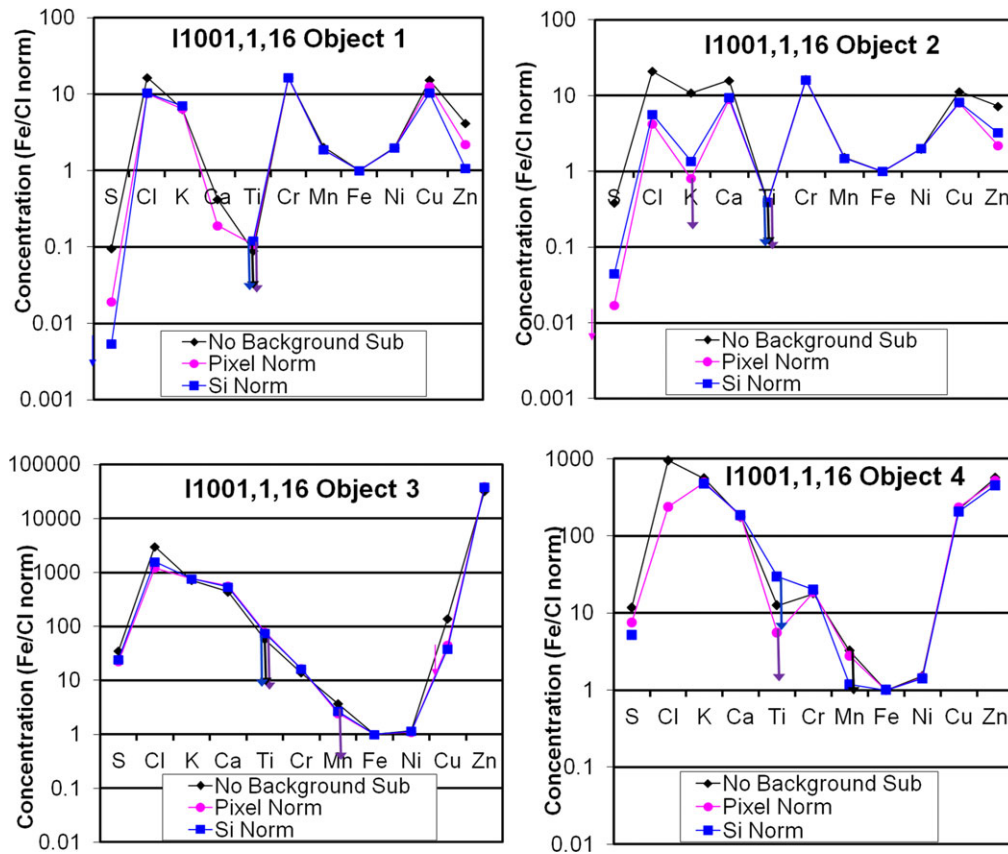


Fig. 6. Chondritic and Fe-normalized element abundance patterns in the four areas from I1001,1,16 identified in Fig. 5. Downward arrows indicate detection limits for elements that were not detected.

it is unclear if Object 1 is a captured particle or a contaminant cast into the aerogel during manufacture.

We also performed XRM element mapping on part of the large fracture in this picokeystone and found an approximately 1 μm feature similar to the Si and Fe hot-spot (Fig. 7) identified as the interstellar candidate. The XRF spectrum for the object in the “fracture” region, i.e., away from the interstellar candidate region, was dominated by Ca, Cr, Fe, Ni, Cu, and Zn with Fe/Ni close to CI, exhibiting a very similar Fe- and Cl-normalized element abundance pattern to that of the Si-rich object in the interstellar candidate area. This similarity of the feature in the crack to the features in the interstellar candidate region suggests that both may have a similar origin, and demonstrates the value of analyzing material well outside the interstellar candidate area to better understand the distribution of elements in the aerogel itself.

Neither Ce nor Al was detected in either of these Si hot-spots, suggesting that they are not secondary fragments from either the solar panels or the aluminum deck.

I1075,1,25

Although a surface feature was identified by the Stardust@Home project, once the interstellar candidate I1075,1,25 picokeystone was extracted, there was no visible track identified by the JSC Curatorial Facility, although several opaque features, possible particles, were visible in this picokeystone. We obtained element maps of part of this picokeystone at low resolution, in 1 μm steps, searching for element hot-spots that might identify a captured particle (Fig. 8a). We identified two Fe hot-spots (spots A and B), located within 20 μm of one another, and two additional Fe hot-spots (spots C and D). These four hot-spots are distributed along an almost straight line that points back to a linear feature at the surface (Fig. 8a). This straight line distribution of material is characteristic of an entry track; however, no track is visible in the optical microscope and no track was imaged in the STXM (Butterworth et al. 2014).

The Fe hot-spots A, B, and C were separately analyzed at high resolution (100 nm step size). The XRM spectra of these particles are easily

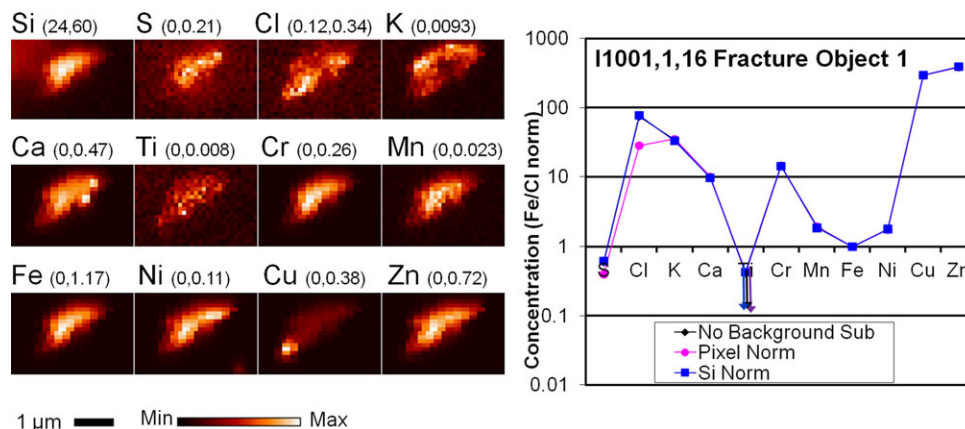


Fig. 7. Element maps (left) and chondritic normalized element/Fe ratios (right) for the Si-rich spot identified along the fracture in I1001,1, 16. Values in parentheses are the minimum and maximum $\mu\text{g cm}^{-2}$ used in applying the color scale bar. Downward arrows indicate detection limits for elements that were not detected.

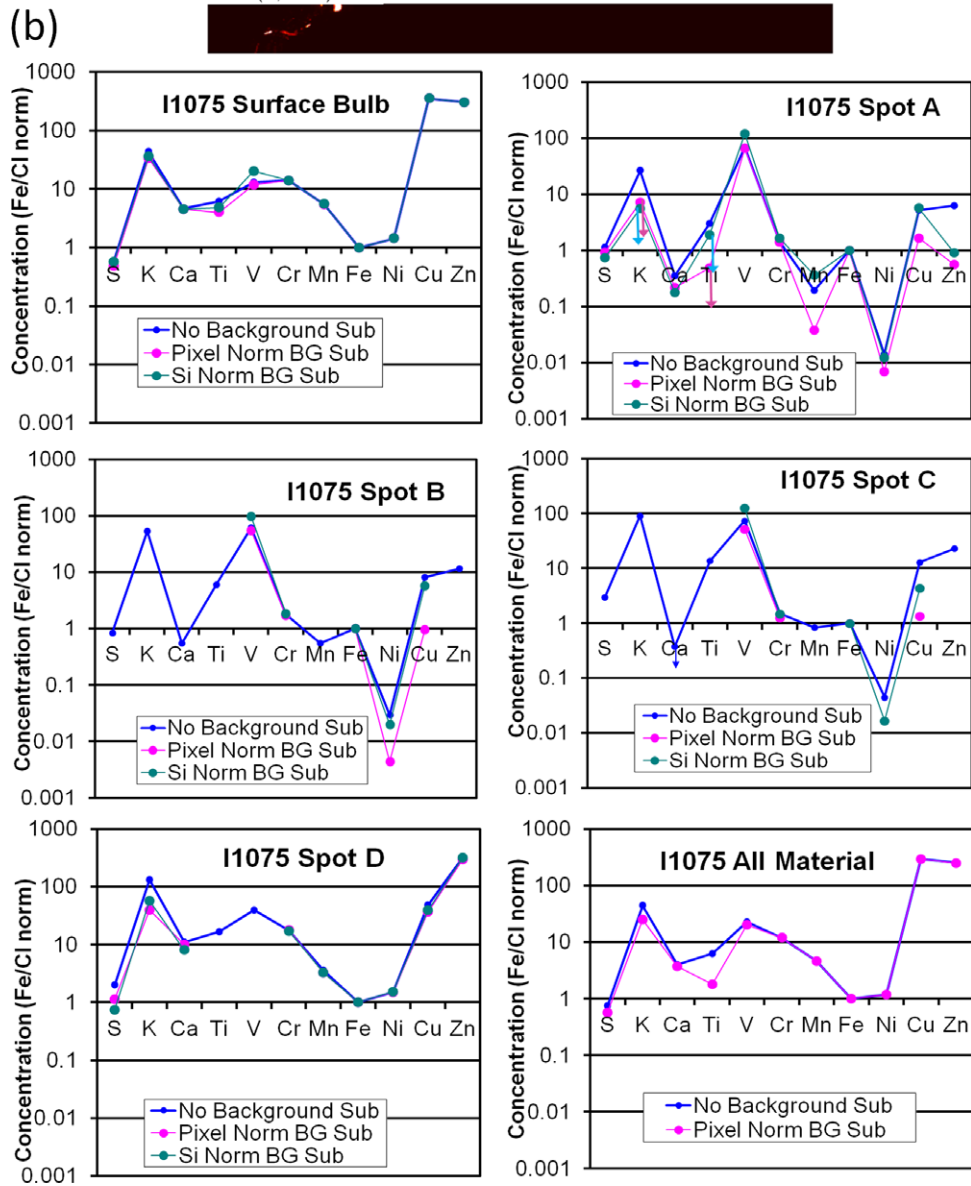
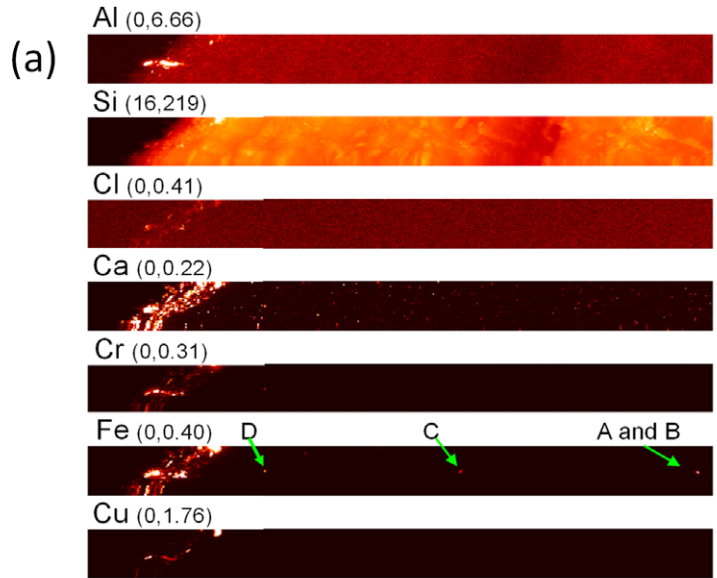
distinguishable from the aerogel background spectrum, with the Ni/Fe ratio significantly lower than CI (Fig. 8b). As there is no track associated with these particles, they are, most likely, contaminants that were cast into the aerogel during its manufacturing process, although we are unable to exclude contaminants emplaced on the surface of the picokeystone during extraction. Spot D, also analyzed at high resolution (100 nm step size), is generally similar in its element to Fe ratios to Spots A, B, and C (Fig. 8b). However, Spot D has a Ni/Fe ratio near the CI value. If, as the absence of a track seems to indicate, Spot D is a contaminant cast into the aerogel during manufacture, this chondritic Ni/Fe ratio indicates that the Ni/Fe ratio cannot be used robustly to distinguish extraterrestrial particles from contaminants in the SIDC.

The surface feature, possibly a bulb or entry hole, was analyzed using the well-defined linear feature in the Al map (Fig. 8a) to define the ROI for the feature. The XRF spectrum of this feature is compared with the spectrum of the aerogel in a feature-free region in Fig. 9. The possible bulb has approximately CI Ni/Fe and S/Fe ratios, but the K/Fe, Ti/Fe, V/Fe, Cr/Fe, Mn/Fe, Cu/Fe, and Zn/Fe ratios are all significantly elevated in this feature (Fig. 8b).

Although we analyzed all the interstellar candidates under the same conditions, resulting in an approximately uniform sensitivity for Al, this is the only one of the six interstellar candidates analyzed at the APS that showed a detectable level of Al in its XRF spectrum (Fig. 9), indicating a very high Al content as the sensitivity for light elements in this XRM is low.

Because parts of the aluminum deck of the Stardust sample return canister were within the field of view of the interstellar aerogel collector during the interstellar collection, we analyzed two samples, H6107-1 and H6107-6, of this aluminum deck material with the XRM on beamline X26A of the National Synchrotron Light Source (Brookhaven National Laboratory, Upton, NY). This XRM has an approximately $7\ \mu\text{m}$ analysis spot. We mapped areas on each of these two samples and found hot-spots of Fe, Ni, and Zn. The element/Fe ratios were determined for an average over each map as well as for each individual hot-spot (Fig. 10). Neither the average over the sampled portion of the aluminum deck material nor any individual hot-spot was an exact match for the material in the Al-rich region of I1075,1,25. However, the abundance pattern of the Al-rich region of I1075,1,25 was similar to the patterns in H6107-6, suggesting that a secondary fragment of the

Fig. 8. a) Element maps, each $160\ \mu\text{m}$ wide, of interstellar candidate I1075,1,25, showing four Fe hot-spots (Spots A, B, C, and D) distributed along a line starting at a surface feature that is most pronounced in the Al, Cr, and Cu maps and visible in the Fe maps as well. Values in parentheses are the minimum and maximum $\mu\text{g cm}^{-2}$ used in applying the color scale bar. b) The chondritic (CI) and Fe-normalized element abundance patterns of Spots A, B, C, D, the surface “bulb,” defined using the hot area in the Al map, and the sum of all material in these five areas on interstellar candidate I1075,1,25. Downward arrows indicate detection limits for elements that were not detected. The abundance pattern of the Al-rich surface feature has an Ni/Fe ratio close to the CI value, but all the other detected elements, except S, are present in ratios to Fe that are well above the CI pattern.



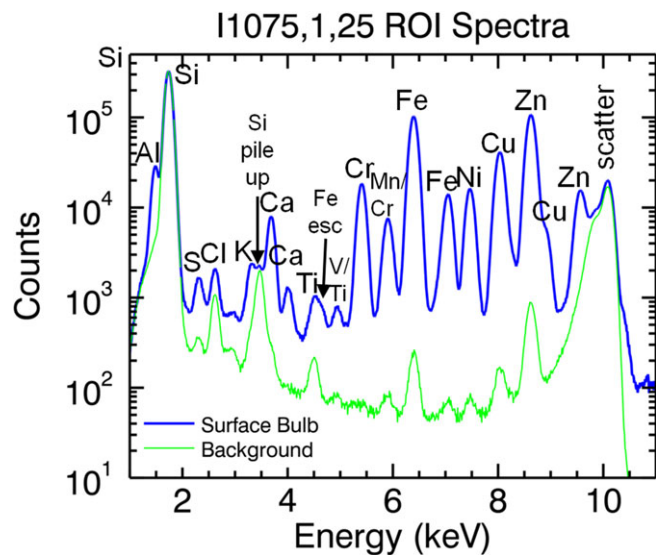


Fig. 9. X-ray fluorescence spectrum of the Al-rich area of I1075,1,25 (blue) compared with the aerogel background spectrum (green) showing that Al, S, V, Cr, Fe, and Cu are easily distinguishable from the aerogel background. The counts in the background spectrum have been scaled to the same number of pixels as the surface bulb spectrum.

aluminum deck material is a likely source of the surface feature in I1075,1,25.

I1004,1,2

The visible light image of I1004,1,2 shows a well-formed, off-normal, carrot track ending at a well-defined terminal particle (Fig. 11). The presence of a terminal particle at the end of a well-developed track

demonstrates that this was a high-speed capture event. Low-resolution XRF maps detected element concentrations (Fig. 11) at the surface of the aerogel (Area 1), in a hot-spot to the left of the track (Area 2), and in the terminal particle (Area 3).

The terminal particle was examined at higher spatial resolution, using a 250 nm step size (Fig. 12). The total Fe mass in the I1004,1,2 terminal particle is 110 fg, which would correspond to an approximately 0.7 μm diameter spherical particle having a CI-like composition and an assumed density of approximately 3 gm cm^{-3} . The Si, S, K, and Cr maps, shown in Fig. 12, indicate that the terminal particle is approximately 3 μm in diameter, which would have a mass more than a factor of 25 greater than the mass inferred for a CI-like Fe concentration, suggesting that the terminal particle is significantly depleted in Fe relative to the CI composition.

The elemental composition of the terminal particle was determined by extracting from the fluorescence map the summed spectra from each of two ROI: a region surrounding the terminal particle and a region of aerogel as far from the terminal particle as possible. The resulting XRF spectra and the abundance patterns are also shown in Fig. 12. The large excess in counts for the terminal particle over the aerogel background, when both are scaled to the same number of pixels, for all elements except Si, demonstrates the detection of these elements associated with the terminal particle.

The CI-normalized abundance pattern of the terminal particle (Fig. 12) shows depletions in Fe and Ca relative to the other detected elements (S, K, Ti, Cr, Mn, Ni, Cu, Zn). The Ni/Fe ratio is >1000 . Although Si, S, K, and Cr are distributed over the

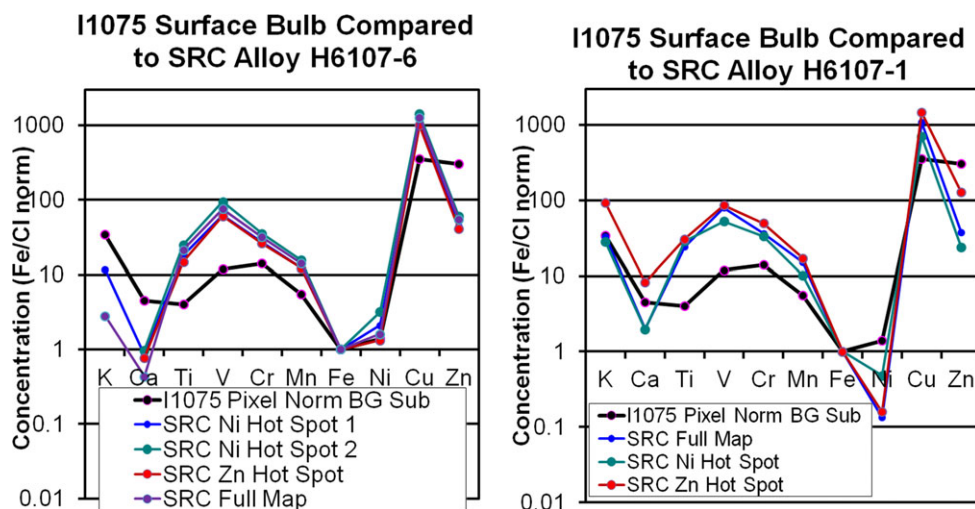


Fig. 10. Comparison of the Fe- and CI-normalized element abundance patterns of the Al-rich region of interstellar candidate I1075,1,25 with two samples of aluminum from the Stardust sample return capsule aluminum deck.

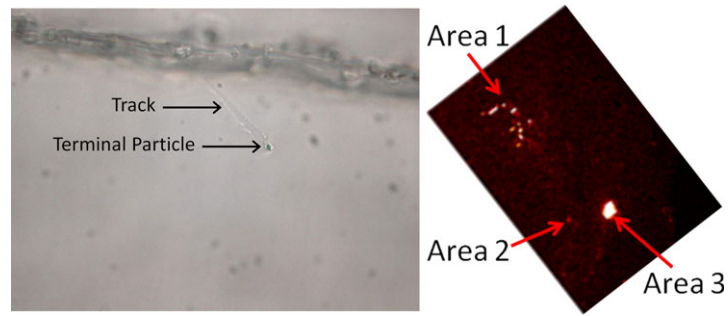


Fig. 11. Left: Visible light image (140 μm width) of interstellar candidate picokeystone I1004,1,2 (from the Stardust Interstellar Preliminary Examination wiki). Right: X-ray fluorescence map of interstellar candidate I1004,1,2 in approximately the same orientation and size scale as the visible light image. The fluorescence map shows concentrations of Fe at the surface of the aerogel (Area 1), a hot-spot to the left of the track (Area 2), and the approximately 3 μm terminal particle (Area 3). In the fluorescence maps, the brightness scales with the element abundance, with the brightest pixels having the highest fluorescence signal for that element.

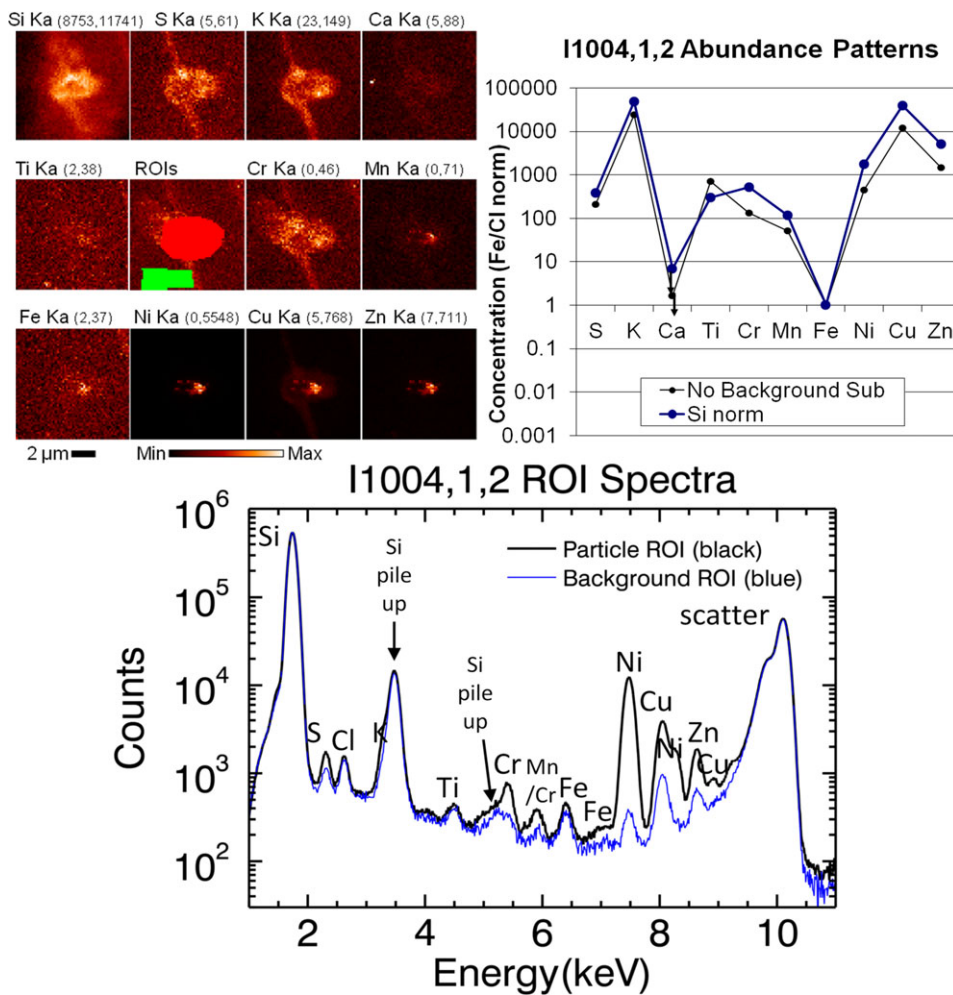


Fig. 12. Interstellar candidate I1004,1,2,0,0. Top left: Individual element fluorescence maps of the particle. Values in parentheses are the minimum and maximum counts used in applying the color scale bar. The “region of interests (ROIs)” image shows the locations of the two integration regions, particle (red) and background (green). Bottom: The resulting integrated X-ray fluorescence spectra of the background region of the aerogel (blue) and the region around the particle (black). The background spectrum was scaled to the Si Ka peak in the particle spectrum. Top right: The Cl- and Fe-normalized element abundance patterns of the particle; no background subtraction in black, Si-normalized background subtraction in blue. Downward arrows indicate detection limits for elements that were not detected. The counts in the background ROI spectrum have been scaled to the same number of pixels as the particle ROI spectrum.

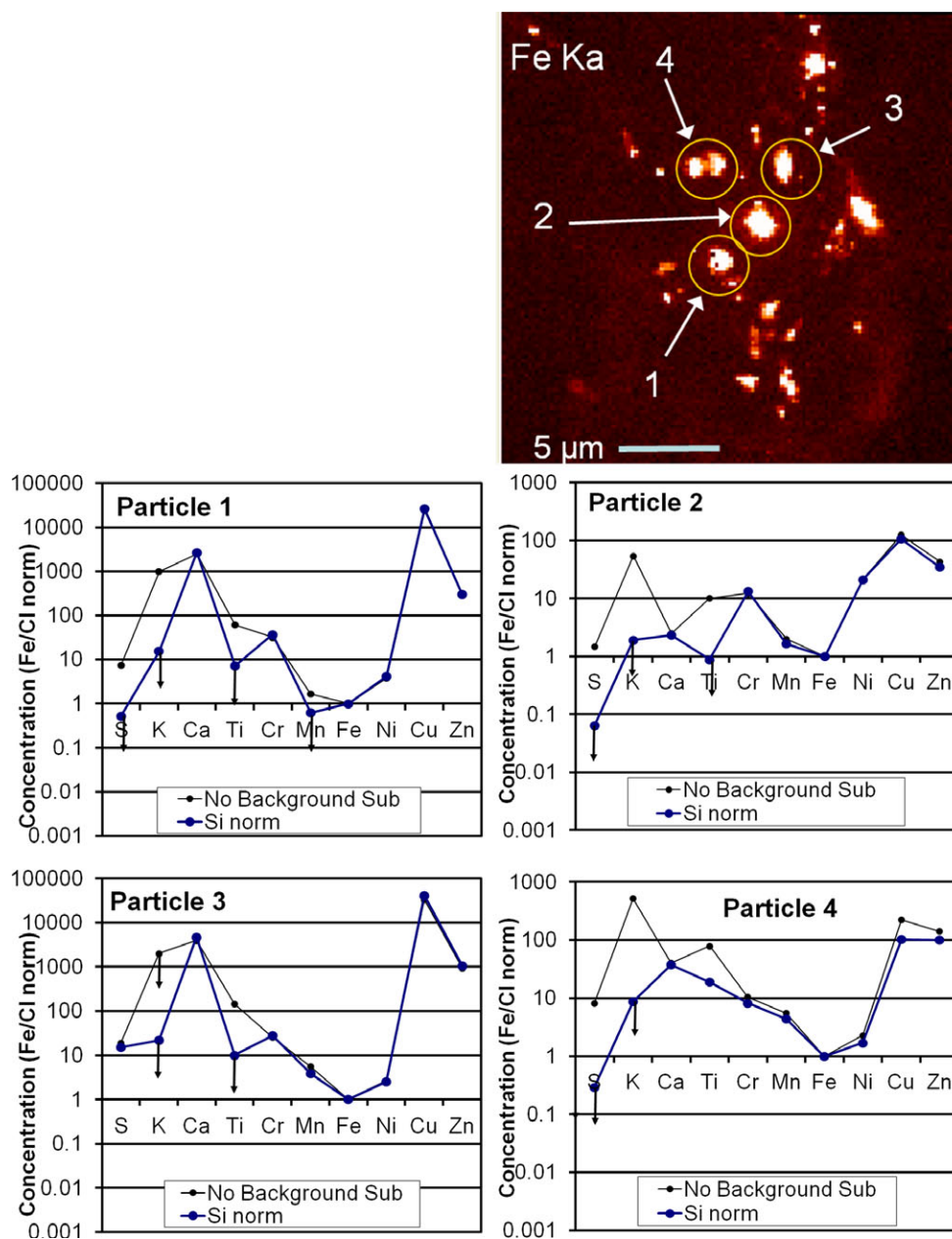


Fig. 13. Interstellar candidate I1004,1,2,0,0. Left: High-resolution Fe element map showing the discrete Fe hot-spots near the surface of the picokeystone. Right and bottom: CI- and Fe-normalized element abundance patterns of four of the brightest Fe hot-spots. Downward arrows indicate detection limits for elements that were not detected.

full approximately 3 μm terminal particle, the Ti, Mn, Fe, Ni, Cu, and Zn are isolated in a small, approximately 500 nm diameter, core region (see Fig. 12).

The Fe map of I1004,1,2 also showed a number of discrete Fe hot-spots near the surface of this picokeystone. We performed element mapping of this region as well, and determined the element/Fe ratios for the four brightest Fe hot-spots (Fig. 13). The element

abundance patterns of these four spots are similar to the pattern we obtained from the terminal particle, suggesting that these spots are material removed from the terminal particle during capture.

Neither the terminal particle nor the discrete Fe hot-spots showed detectable Ce, indicating that they are not contaminants from the solar cells.

Although we failed to detect Al in the XRM, the sensitivity of this hard XRM drops rapidly for low-Z

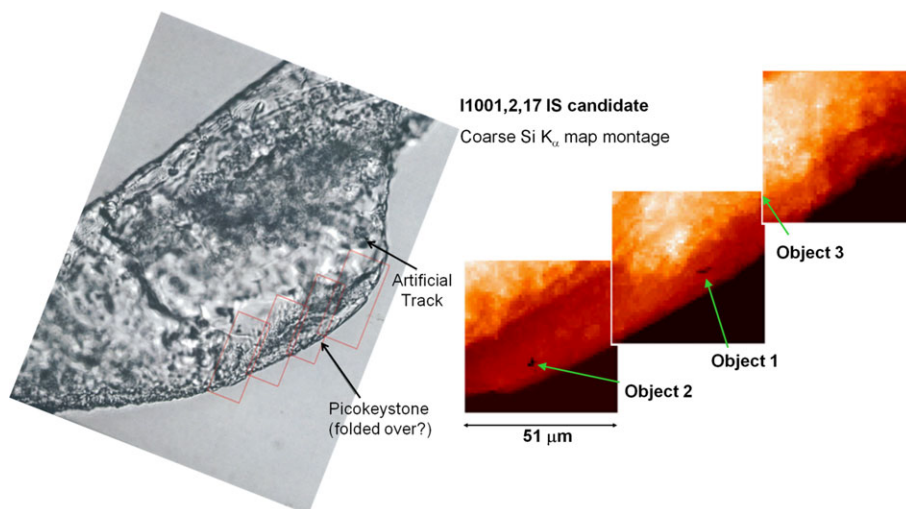


Fig. 14. Left: Visible light microscope image (900 μm width) of interstellar picokeystone I1001,2,17, showing the picokeystone folded over onto the thicker keystone section. Right: X-ray fluorescence Si map of the edge of the picokeystone, showing three low-Si (dark) regions.

elements (see Fig. 1). STXM measurements indicate that the terminal particle contains approximately 1.8 pg of Al (Butterworth et al. 2014), giving an Al/Fe ratio of approximately 16, about one-fourth the value we found in the Al-rich bulb of I1075,1,25. The high Ni/Fe ($>1000 \times \text{CI}$) in the terminal particle is quite different from the Ni/Fe we found in either the Stardust aluminum deck material (Fig. 10), where even the Ni hot-spots had Ni/Fe $<6 \times \text{CI}$, or the Al-rich bulb of I1075,1,25 (Fig. 9). But inhomogeneity in the Stardust aluminum deck material leaves open the possibility that I1004,1,2 is a secondary produced by an impact on the aluminum deck. An impact producing an approximately 3 μm secondary should be accompanied by additional secondaries, possibly in the micron to submicron size, which have not been reported in this aerogel cell or the foils adjacent to this aerogel cell. Alternatively, as ancient interstellar dust with a diverse variety of compositions and mineralogies has been identified in meteorites, an interstellar or interplanetary origin for this particle cannot be excluded based solely on its composition.

I1001,2,17

I1001,2,17 was received at the APS with the picokeystone portion curled over the thicker keystone section (Fig. 14). No track or particles were visible in an optical microscope examination of this picokeystone. We mapped the picokeystone region using the XRM and identified three low Si regions, ranging from 1 to 5 μm in size, which were analyzed

at higher resolution (Fig. 15). Object 1 had approximately CI Cr/Fe and Ni/Fe, but large enrichments in most of the other elements were detected. The other two had very low Ni/Fe, less than 1/100th the CI ratio as well as low S, Ca, Ti, Cr, Mn, and Zn (Fig. 15). As the aerogel itself has an Ni/Fe ratio greater than the CI value, the low Ni/Fe in Spots 2 and 3 indicates that these low Si spots are not consistent with simply the background contamination in the aerogel. Because the picokeystone overlays the thicker keystone, we were not able to determine if the low Si regions are in the picokeystone or the underlying keystone.

I1044,2,32

I1044,2,32 was also received with the picokeystone curled over the thicker keystone (Fig. 16). Again, no track or particles were visible in optical microscope examination. The XRF map of the candidate region showed only a single approximately 5 μm Si hot-spot. The spectrum of this Si rich region was quite similar to the aerogel itself, consistent with higher density aerogel. The high-resolution map showed a small Fe-Ni hot-spot outside the Si enriched region (Fig. 16). The integrated spectrum for this small particle showed only Fe and Ni, with Ni/Fe approximately $60 \times \text{CI}$, detectable above the aerogel background. There is no evidence of a track, possibly due to the curling of the aerogel, but it seems likely that this Fe hot-spot is simply a submicron Fe-Ni-bearing contaminant in the aerogel.

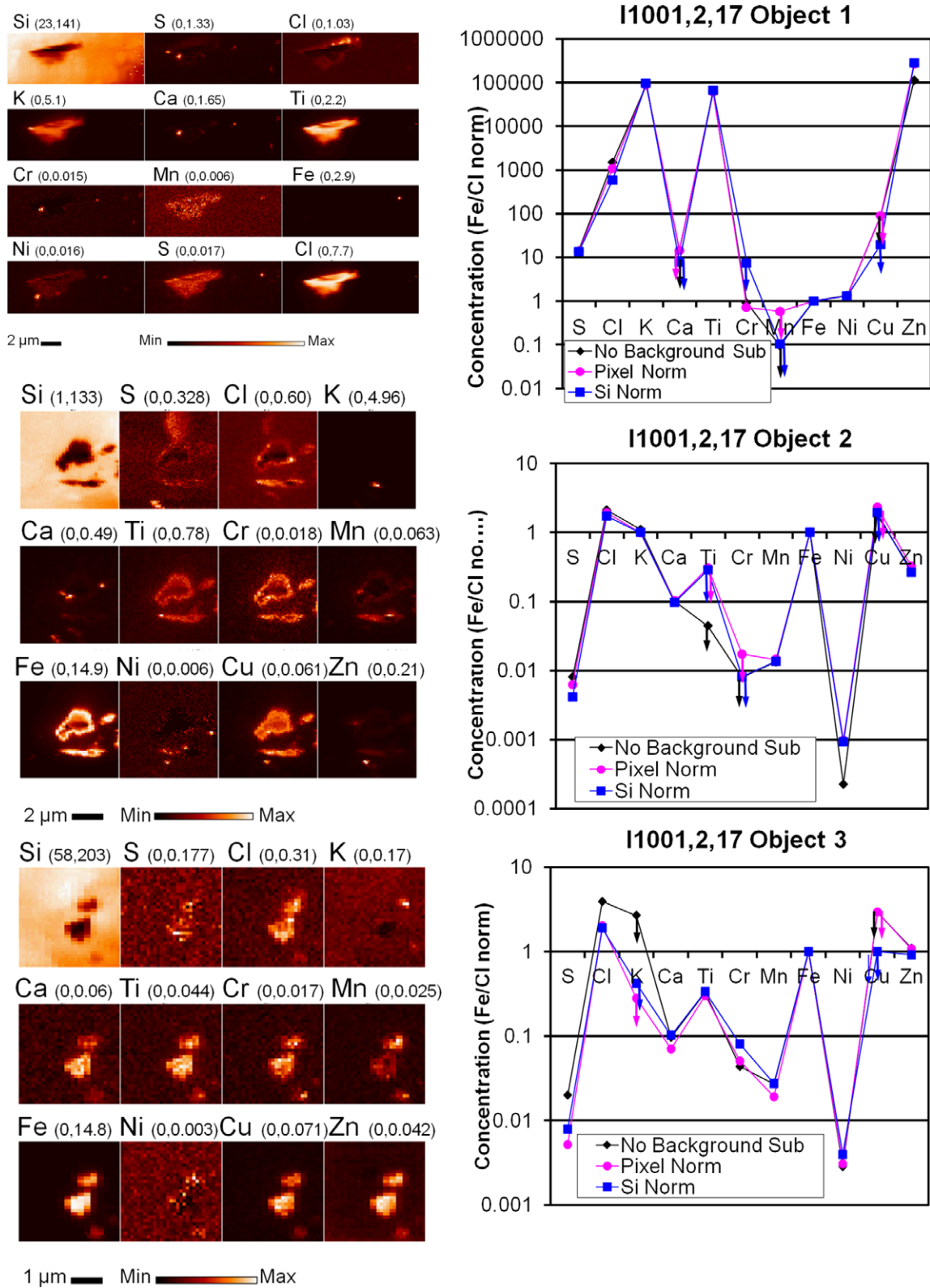


Fig. 15. Left: X-ray fluorescence element maps of the three low-Si regions of I1001,2,17 (Objects 1, 2, and 3 from top). Values in parentheses are the minimum and maximum $\mu\text{g cm}^{-2}$ used in applying the color scale bar. Right: the Cl- and Fe-normalized element abundance patterns for each region (Objects 1, 2, and 3 from top). Downward arrows indicate region (Objects 1, 2, and 3 from top). Downward arrows indicate detection limits for elements that were not detected.

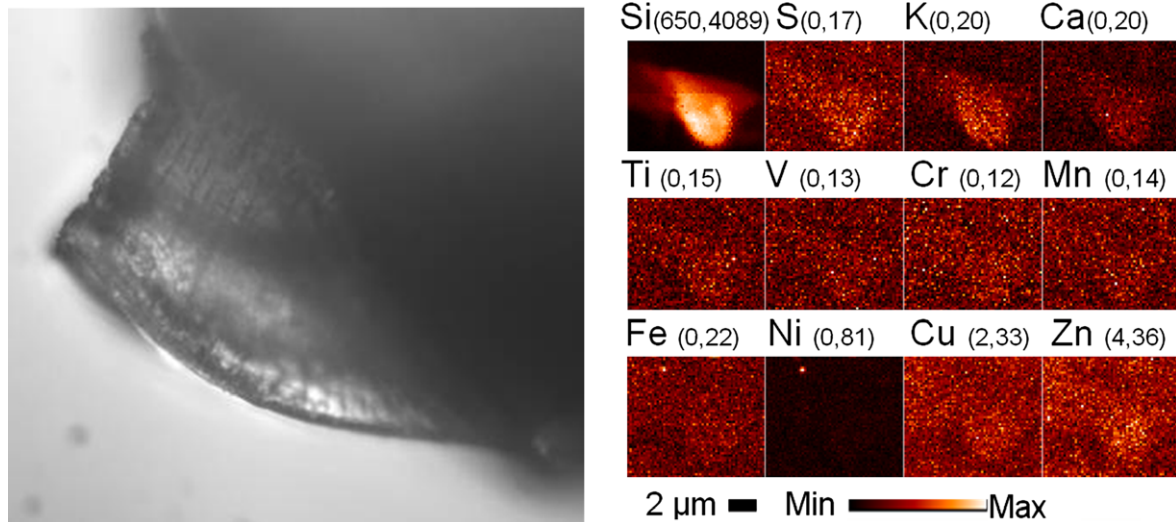


Fig. 16. Left: Visible light microscope image (320 μm width) of interstellar candidate I1044,2,32 showing the curled edge of the picokeystone. Right: X-ray fluorescence element maps showing the high-Si area, and a single, submicron high-Ni spot just outside of the high-Si area. Values in parentheses are the minimum and maximum counts used in applying the color scale bar.

CONCLUSIONS

Our results demonstrate the utility of synchrotron XRF as a preliminary screening tool to determine the abundances for elements with $Z \geq 19$ (K) in submicron particles embedded in Stardust aerogel. These XRF measurements can be used to identify spacecraft secondaries in the Stardust interstellar aerogel based on similarity in composition to the measured compositions of the solar panels and aluminum deck, and to identify interstellar candidates, even those submicron in diameter, exhibiting compositions consistent with interstellar or interplanetary dust, which require further analysis by other techniques.

Among the six interstellar candidates we analyzed, only the surface feature in I1044,3,33 has an approximately chondritic element abundance pattern. Except for the elevated K and Zn and low S, this element abundance pattern is consistent with the expected mean composition of an approximately 350 nm interstellar or interplanetary dust particle. This surface feature is consistent with the impact of a weak high-speed particle. As this feature was not detected in the Stardust@Home optical scanning of the aerogel cell, if it was produced by the impact of an interstellar or interplanetary dust particle, then the Stardust@Home optical scanning may be inadequate to identify all impact features produced by particles in the expected interstellar size range. This suggests that the optical search for interstellar candidates should be supplemented with other search techniques.

Only one of the six interstellar candidates, I1004,1,2, showed an obvious track with a terminal

particle. In comparison with CI, the terminal particle in I1004,1,2 is depleted in Fe and Ca relative to the other detected elements (S, K, Ti, Cr, Mn, Ni, Cu, Zn). This element abundance pattern does not match the composition of any of the analyzed spots of the Stardust spacecraft components that were in the field of view of the SIDC, but the high Al/Fe ratio suggests the Al-deck of the Stardust sample return capsule as a possible source. An interplanetary or interstellar origin for the terminal particle cannot be excluded by our measurements.

In both I1044,3,33 and I1004,1,2, we detected no Ce, the expected signature of secondary fragments produced by impacts into the Stardust solar panels. The origin of the terminal particle in I1004,1,2 and the surface feature in I1044,3,33 cannot be established based solely on these elemental analyses.

A third interstellar candidate, I1075,1,25, showed an Al-rich surface feature with a composition generally consistent with the composition of aluminum deck material of the Stardust sample return capsule, which was in a position to contribute secondary ejecta to the SIDC.

Although Fe is expected to be a major element in interstellar dust, our measurements demonstrate the presence of Fe hot-spots, presumably contamination, as they were in or on the surface of the picokeystones but not associated with tracks, which complicates any search for interstellar particles by Fe-mapping techniques. In addition, although the Ni/Fe ratio is generally a good discriminator between primitive extraterrestrial materials, with Ni/Fe approximately 1/18, and natural terrestrial materials, with much lower Ni/Fe, we identified

submicron contaminants in or on the surfaces of the Stardust interstellar aerogel picokeystone with Ni/Fe ranging from approximately $60 \times$ CI to less than 1/100th CI, demonstrating that the Stardust aerogel contains man-made contaminants with Ni/Fe near or above the CI value, precluding the use of the Ni/Fe ratio as an identifier of extraterrestrial particles.

Acknowledgments—The Stardust interstellar dust collection mission was supported by NASA as the fourth mission in the Discovery program. This analytical work was supported by a NASA Laboratory Analysis of Returned Samples research grant NNX11AE15G (to G. J. F.). Use of the Advanced Photon Source, an Office of Science User Facility operated for the U.S. Department of Energy (DOE) Office of Science by Argonne National Laboratory, was supported by the U.S. DOE under Contract No. DE-AC02-06CH11357. Portions of this work were performed at Beamline X26A, National Synchrotron Light Source (NSLS), Brookhaven National Laboratory. X26A is supported by the Department of Energy (DOE)—Geosciences (DE-FG02-92ER14244 to The University of Chicago—CARS). Use of the NSLS was supported by DOE under Contract No. DE-AC02-98CH10886.

Editorial Handling—Dr. Christian Koeberl

REFERENCES

- Brownlee D., Tsou P., Aléon J., Alexander C. M. O'D., Araki T., Bajt S., Baratta G. A., Bastien R., Bland P., Bleuet P., Borg J., Bradley J. P., Brearley A., Brenker F., Brennan S., Bridges J. C., Browning N. D., Brucato J. R., Bullock E., Burchell M. J., Busemann H., Butterworth A., Chaussidon M., Chevront A., Chi M., Cintala M. J., Clark B. C., Clemett S. J., Cody G., Colangeli L., Cooper G., Cordier P., Daghlian C., Dai Z., D'Hendecourt L., Djouadi Z., Dominguez G., Duxbury T., Jason J. P., Ebel D. S., Economou T. E., Fakra S., Fairey S. A. J., Fallon S., Ferrini G., Ferroir T., Fleckenstein H., Floss C., Flynn G. J., Franchi I. A., Fries M., Gainsforth Z., Gallien J.-P., Genge M., Gilles M. K., Gillet P., Gilmour J., Glavin D. P., Gounelle M., Grady M. M., Graham G. A., Grant P. G., Green S. F., Grossemy F., Grossman L., Grossman J. N., Guan Y., Hagiya K., Harvey R., Heck P., Herzog G. F., Hoppe P., Hörz F., Huth J., Hutcheon I. D., Ignatyev K., Ishii H., Jacob D., Jacobsen C., Jacobsen S., Jones S., Joswiak D., Jurewicz A., Kearsley A., Keller L. P., Khodja H., Kilcoyne A. L. D., Kissel J., Krot A., Langenhorst F., Lanzirotti A., Le L., Leshin L. A., Leitner J., Lemelle L., Leroux H., Liu M.-C., Luening K., Lyon I., MacPherson G., Marcus M. A., Marhas K., Marty B., Matrajt G., McKeegan K., Meibom A., Mennella V., Messenger K., Messenger S., Mikouchi T., Mostefaoui S., Nakamura T., Nakano T., Newville M., Nittler L. R., Ohnishi I., Ohsumi K., Okudaira K., Papanastassiou D. A., Palma R., Palumbo M. E., Pepin R. O., Perkins D., Perronnet M., Pianetta P., Rao W., Rietmeijer F. J. M., Robert F., Rost D., Rotundi A., Ryan R., Sandford S. A., Schwandt C. S., See T. H., Schlutter D., Sheffield-Parker J., Simionovici A., Simon S., Sitnitsky I., Snead C. J., Spencer M. K., Stadermann F. J., Steele A., Stephan T., Stroud R., Susini J., Sutton S. R., Suzuki Y., Taheri M., Teslich S., Tomeoka K., Tomioka N., Toppani A., Trigo-Rodríguez J. M., Troadec D., Tsuchiyama A., Tuzzolino A. J., Tylliszczak T., Uesugi K., Velbel M., Vellenga J., Vicenzi E., Vincze L., Warren J., Weber I., Weisberg M., Westphal A. J., Wirick S., Wooden D., Wopenka B., Wozniakiewicz P., Wright I., Yabuta H., Yano H., Young E. D., Zare R. N., Zega T., Ziegler K., Zimmerman L., Zinner E., and Zolensky M. E. 2006. Comet 81P/Wild 2 under a microscope. *Science* 314:1711–1716.
- Butterworth A. L., Westphal A. J., Tylliszczak T., Gainsforth Z., Stodolna J., Frank D. R., Allen C., Anderson D., Ansari A., Bajt S., Bastien R. S., Bassim N., Bechtel H. A., Borg J., Brenker F. E., Bridges J., Brownlee D. E., Burchell M., Burghammer M., Changela H., Cloetens P., Davis A. M., Doll R., Floss C., Flynn G., Grün E., Heck P. R., Hillier J. K., Hoppe P., Hudson B., Huth J., Hvide B., Kearsley A., King A. J., Lai B., Leitner J., Lemelle L., Leroux H., Leonard A., Lettieri R., Marchant W., Nittler L. R., Ogliore R., Ong W. J., Postberg F., Price M. C., Sandford S. A., Sans Tresseras J., Schmitz S., Schoonjans T., Silversmit G., Simionovici A. S., Solé V. A., Srama R., Stephan T., Sterken V. J., Stroud R. M., Sutton S., Trierloff M., Tsou P., Tsuchiyama A., Vekemans B., Vincze L., Korff J. V., Wordsworth N., Zevin D., Zolensky M. E., and >30,000 Stardust@home dusters. 2014. Stardust Interstellar Preliminary Examination IV: Scanning transmission X-ray microscopy analyses of impact features in the Stardust Interstellar Dust Collector. *Meteoritics & Planetary Science* 48, doi:10.1111/maps.12220.
- Clayton D. D. and Nittler L. R. 2004. Astrophysics with presolar stardust. *Annual Review of Astronomy and Astrophysics* 42:39–78.
- Flynn G. J., Bleuet P., Borg J., Bradley J. P., Brenker F. E., Brennan S., Bridges J., Brownlee D. E., Bullock E. S., Burghammer M., Clark B. C., Dai Z. R., Daghlian C. P., Djouadi Z., Fakra S., Ferroir T., Floss C., Franchi I. A., Gainsforth Z., Gallien J.-P., Gillet P., Grant P. G., Graham G. A., Green S. F., Grossemy F., Heck P. R., Herzog G. F., Hoppe P., Hörz F., Huth J., Ignatyev K., Ishii H. A., Janssens K., Joswiak D., Kearsley A. T., Khodja H., Lanzirotti A., Leitner J., Lemelle L., Leroux H., Luening K., MacPherson G. J., Marhas K. K., Marcus M. A., Matrajt G., Nakamura T., Nakamura-Messenger K., Nakano T., Newville M., Papanastassiou D. A., Pianetta P., Rao W., Riekel C., Rietmeijer F. J. M., Rost D., Schwandt C. S., See T. H., Sheffield-Parker J., Simionovici A., Sitnitsky I., Snead C. J., Stadermann F. J., Stephan T., Stroud R. M., Susini J., Suzuki Y., Sutton S. R., Taylor S., Teslich N., Troadec D., Tsou P., Tsuchiyama A., Uesugi K., Vekemans B., Vicenzi E. P., Vincze L., Westphal A. J., Wozniakiewicz P., Zinner E., and Zolensky M. E. 2006. Elemental compositions of comet 81P/Wild 2 samples collected by Stardust. *Science* 314:1731–1734.
- Flynn G., Sutton S., and Lanzirotti A. 2009. A synchrotron-based facility for the in-situ location, chemical and

- mineralogical characterization of ~10 μm particles captured in aerogel. *Advances in Space Research* 43:328–334.
- Frank D. R., Westphal A. J., Zolensky M. E., Bastien R. K., Gainsforth Z., Allen C., Anderson D., Ansari A., Bajt S., Bassim N., Bechtel H. A., Borg J., Brenker F. E., Bridges J., Brownlee D. E., Burchell M., Burghammer M., Butterworth A. L., Changela H., Cloetens P., Davis A. M., Doll R., Floss C., Flynn G., Grün E., Heck P. R., Hillier J. K., Hoppe P., Hudson B., Huth J., Hvide B., Kearsley A., King A. J., Lai B., Leitner J., Lemelle L., Leroux H., Leonard A., Lettieri R., Marchant W., Nittler L. R., Oglione R., Ong W. J., Postberg F., Price M. C., Sandford S. A., Sans Tresseras J., Schmitz S., Schoonjans T., Silversmit G., Simionovici A. S., Solé V. A., Srama R., Stephan T., Sterken V. J., Stroud R. M., Sutton S., Trieloff M., Tsou P., Tsuchiyama A., Vekemans B., Vincze L., Korff J. V., Wordsworth N., Zevin D., and >30,000 Stardust@home dusters. 2013. Stardust Interstellar Preliminary Examination II: Curating the Stardust interstellar dust collector, picokeystones, and sources of impact tracks. *Meteoritics & Planetary Science* 48, doi:10.1111/maps.12147.
- Jones A. P., Tielens A. G. G. M., and Hollenbach D. J. 1996. Grain shattering in shocks: The interstellar grain size distribution. *The Astrophysical Journal* 469:740–764.
- Kemper F., Vriend W. J., and Tielens A. G. G. M. 2004. The absence of crystalline silicates in the diffuse interstellar medium. *The Astrophysical Journal* 609:826–837.
- Krüger H., Landgraf M., Altobelli N., and Grün E. 2007. Interstellar dust in the solar system. *Space Science Reviews* 130:401–408.
- Lodders K. 2003. Solar system abundances and condensation temperatures of the elements. *The Astrophysical Journal* 591:1220–1247.
- Messenger S., Keller L. P., and Lauretta D. S. 2005. Supernova olivine from cometary dust. *Science* 309:737–741.
- Postberg F., Hillier J. K., Armes S. P., Bugiel S., Butterworth A. L., Dupin D., Fielding L. A., Fujii S., Gainsforth Z., Grün E., Li Y. W., Srama R., Sterken V. J., Stodolna J., Trieloff M., Westphal A. J., Allen C., Anderson D., Ansari A., Bajt S., Bastien R. S., Bassim N., Bechtel H. A., Borg J., Brenker F. E., Bridges J., Brownlee D. E., Burchell M., Burghammer M., Changela H., Cloetens P., Davis A. M., Doll R., Floss C., Flynn G., Frank D. R., Heck P. R., Hoppe P., Hudson B., Huth J., Hvide B., Kearsley A., King A. J., Lai B., Leitner J., Lemelle L., Leroux H., Leonard A., Lettieri R., Marchant W., Nittler L. R., Oglione R., Ong W. J., Postberg F., Price M. C., Sandford S. A., Sans Tresseras J., Schmitz S., Schoonjans T., Silversmit G., Simionovici A. S., Solé V. A., Stephan T., Sterken V. J., Stroud R. M., Sutton S., Trieloff M., Tsou P., Tsuchiyama A., Tylliszczak T., Vekemans B., Vincze L., Korff J. V., Wordsworth N., Zevin D., Zolensky M. E., and >30,000 Stardust@home dusters. 2014. Stardust Interstellar Preliminary Examination IX: High speed interstellar dust analog capture in Stardust flight-spore aerogel. *Meteoritics & Planetary Science* 48, doi:10.1111/maps.12173.
- Savage B. D. and Sembach K. R. 1996. Interstellar abundances from absorption-line observations with the Hubble Space Telescope. *Annual Review of Astronomy and Astrophysics* 34:279–329.
- Sterken V. J., Westphal A. J., Altobelli N., Grün E., Hillier J. K., Postberg F., Srama R., Allen C., Anderson D., Ansari A., Bajt S., Bastien R. S., Bassim N., Bechtel H. A., Borg J., Brenker F. E., Bridges J., Brownlee D. E., Burchell M., Burghammer M., Butterworth A. L., Changela H., Cloetens P., Davis A. M., Doll R., Floss C., Flynn G., Frank D., Gainsforth Z., Heck P. R., Hoppe P., Hudson B., Huth J., Hvide B., Kearsley A., King A. J., Lai B., Leitner J., Lemelle L., Leroux H., Leonard A., Lettieri R., Marchant W., Nittler L. R., Oglione R., Ong W. J., Price M. C., Sandford S. A., Tresseras J. S., Schmitz S., Schoonjans T., Silversmit G., Simionovici A., Solé V. A., Stephan T., Stodolna J., Stroud R. M., Sutton S., Trieloff M., Tsou P., Tsuchiyama A., Tylliszczak T., Vekemans B., Vincze L., Korff J. V., Wordsworth N., Zevin D., Zolensky M. E., and >30,000 Stardust@home dusters. 2014. Stardust Interstellar Preliminary Examination X: Impact speeds and directions of interstellar grains on the Stardust dust collector. *Meteoritics & Planetary Science* 48, doi:10.1111/maps.12219.
- Sutton S. R. and Flynn G. J. 1988. Stratospheric particles: Synchrotron X-ray fluorescence determination of trace element contents. Proceedings, 18th Lunar and Planetary Science Conference. Houston, TX: Lunar & Planetary Institute. pp. 607–614.
- Twining B. S., Baines S. B., Fisher N. S., Maser J., Vogt S., Jacobsen C., Tovar-Sanchez A., and Sanudo-Wilhelmy S. A. 2003. Quantitative trace elements in individual aquatic protist cells with a synchrotron X-ray fluorescence microprobe. *Analytical Chemistry* 75:3806–3816.
- Westphal A. J., Anderson D., Butterworth A. L., Frank D. R., Hudson B., Lettieri R., Marchant W., Korff J. V., Zevin D., Ardizzone A., Campanile A., Capraro M., Courtney K., Crumpler D., Cwik R., Gray F. J., Imada G., Karr J., Lau Wan Wah L., Mazzucato M., Motta P. G., Spencer R. C., Woodrough S. B., Santoni I. C., Sperry G., Terry J., Wordsworth N., Yanke T. Sr., Ansari A., Bajt S., Bastien R. S., Bassim N., Bechtel H. A., Borg J., Brenker F. E., Bridges J., Brownlee D. E., Burchell M., Burghammer M., Changela H., Cloetens P., Davis A. M., Doll R., Floss C., Flynn G., Gainsforth Z., Grün E., Heck P. R., Hoppe P., Huth J., Hvide B., Kearsley A., King A. J., Lai B., Leitner J., Lemelle L., Leroux H., Nittler L. R., Oglione R., Ong W. J., Price M. C., Sandford S. A., Tresseras J. S., Schmitz S., Schoonjans T., Silversmit G., Simionovici A., Solé V. A., Stephan T., Stodolna J., Stroud R. M., Sutton S., Trieloff M., Tsou P., Tsuchiyama A., Tylliszczak T., Vekemans B., Vincze L., Zolensky M. E., and >30,000 Stardust@home dusters. 2014a. Stardust Interstellar Preliminary Examination I: Identification of tracks in aerogel. *Meteoritics & Planetary Science* 48, doi:10.1111/maps.12168.
- Westphal A. J., Bechtel H. A., Brenker F. E., Butterworth A. L., Flynn G., Frank D. R., Gainsforth Z., Hillier J. K., Postberg F., Simionovici A. S., Sterken V. J., Stroud R. M., Allen C., Anderson D., Ansari A., Bajt S., Bastien R. S., Bassim N., Borg J., Bridges J., Brownlee D. E., Burchell M., Burghammer M., Changela H., Cloetens P., Davis A. M., Doll R., Floss C., Grün E., Heck P. R., Hoppe P., Hudson B., Huth J., Hvide B., Kearsley A., King A. J., Lai B., Leitner J., Lemelle L., Leroux H., Leonard A., Lettieri R., Marchant W., Nittler L. R., Oglione R., Ong W. J., Price M. C., Sandford S. A., Sans Tresseras J., Schmitz S.,

- Schoonjans T., Silversmit G., Solé V. A., Srama R., Stephan T., Stodolna J., Sutton S., Trieloff M., Tsou P., Tsuchiyama A., Tyliczszak T., Vekemans B., Vincze L., Korff J. V., Wordsworth N., Zevin D., Zolensky M. E., and >30,000 Stardust@home dusters. 2014b. Final reports of the Stardust Interstellar Preliminary Examination. *Meteoritics & Planetary Science* 48, doi:10.1111/maps.12221.
- Whittet D. C. B., Boogert A. C. A., Gerakines P. A., Schutte W., Tielens A. G. G. M., de Graauw T., Prusti T., van Dishoeck E. F., Wesselius P. R., and Wright C. M. 1997. Infrared spectroscopy of dust in the diffuse interstellar medium toward Cygnus OB2 No. 12. *The Astrophysical Journal* 490:729–734.
- Wilson T. L. 1999. Isotopes in the interstellar medium and in circumstellar envelopes. *Reports on Progress in Physics*, 62:143–185.
- Zhukovska S., Gail H.-P., and Trieloff M. 2008. Evolution of interstellar dust and stardust in the solar neighborhood. *Astronomy & Astrophysics* 479:453–480.
-